Journal of Alloys and Compounds 1049 (2025) 185342

Contents lists available at ScienceDirect

Journal of Alloys and Compounds

journal homepage: www.elsevier.com/locate/jalcom

Thermodynamics-guided high-throughput discovery of magnetic high-entropy alloys fabricated by spark plasma sintering at different temperatures

Jon Mikel Sanchez [a,*], Miguel A. Lagos [a], Jose Carlos Garcia [a], Iñaki Leizaola [a], Blanca Luna Checa Fernández [a], Christian Rivera [b]

[a] *TECNALIA, Basque Research and Technology Alliance (BRTA), Donosti 20009, Spain*
[b] *Faculty of Engineering, Mondragon Unibertsitatea, Mondragón 20500, Spain*

ARTICLE INFO

Keywords:
High-throughput calculations
High-entropy alloy
CALPHAD
Thermodynamics
Microstructure
Magnetic properties
Spark plasma sintering

ABSTRACT

This study presents a high-throughput, thermodynamics-guided framework for the discovery of novel magnetic high-entropy alloys (HEA). High-throughput CALPHAD simulations were employed to predict the equilibrium phases and Curie temperatures across a broad compositional space, including benchmark systems. The computational results were integrated with statistical data analysis to identify candidate compositions with optimal magnetic properties. The selected $Fe_{42}Co_{17}Ni_{12}Al_{17}Cu_6Ti_6$ HEA was fabricated by spark plasma sintering at various temperatures. For direct comparison, a reference Alnico 5 alloy was synthesized under the same processing conditions at 1273 K. The as-sintered HEA exhibited superior magnetic properties, with a maximum energy product (BH_{max}) of 4.4 kJ/m^3 and coercivities (H_{cj} = 35.7 kA/m, H_{cb} = 33.4 kA/m) exceeding those of the Alnico 5 benchmark (BH_{max} = 3.3 kJ/m^3, H_{cj} = 30.3 kA/m, H_{cb} = 27.9 kA/m). Furthermore, the HEA exhibited superior thermal stability, maintaining its remanence with a more gradual decline up to 1030 K, in contrast to Alnico 5, which underwent a rapid decrease above 870 K. This work establishes a versatile approach for accelerating the design of sustainable magnetic materials with tailored properties, effectively bridging high-throughput thermodynamic modeling and advanced manufacturing.

1. Introduction

High-entropy alloys (HEAs) have emerged as a transformative class of materials, distinguished by their equiatomic or near-equiatomic multicomponent compositions [1]. While their exceptional mechanical properties such as high strength, hardness, and corrosion resistance have been extensively explored for structural applications [2–4], their potential as functional materials, particularly in magnetism, remains underexplored [5–8]. This gap is critical given the urgent global imperative to decarbonize energy systems and achieve net-zero emissions by 2050 [9]. Magnetic materials are central to this transition, serving as indispensable components in technologies such as electric vehicle motors, wind turbine generators, and energy-efficient sensors [10]. However, conventional magnetic alloys often rely on scarce, geopolitically sensitive, or environmentally damaging rare-earth elements, highlighting the need for sustainable alternatives [11,12].

HEAs offer a promising alternative by combining tunable magnetic properties with a reduced reliance on critical resources. Their vast compositional space enables precise tailoring of phase transformations (e.g., spinodal decomposition, nanoprecipitation) and magnetic behavior through elemental selection and processing optimization. For instance, Yu et al. [13] demonstrated the tunability of magnetic properties in equiatomic CoCrFeCuNi and CoCrFeMnNi alloys. Both systems exhibited soft magnetic behavior, but saturation magnetization (M_s) varied significantly as a direct result of substituting Cu with Mn. Similarly, Liu et al. [14] found that the composition and phase constitution affected the soft magnetic performance of $AlCoCuFeNi_x$ HEAs. Adjusting the Ni content enabled the $AlCoCuFeNi_{1.5}$ alloy to achieve an optimal balance of mechanical and magnetic properties, while the $AlCoCuFeNi_{0.5}$ alloy exhibited a high Curie temperature (T_c) above 900 K and strong phase stability below 1350 K.

Other studies have proposed advanced design strategies for specific applications. Han et al. proposed a Fe-Co-Ni-Ta-Al-based HEA for soft magnetic components operating at elevated temperatures. The

---

[*] Corresponding author.
E-mail address: jonmikel.sanchez@tecnalia.com (J.M. Sanchez).

https://doi.org/10.1016/j.jallcom.2025.185342
Received 16 April 2025; Received in revised form 27 November 2025; Accepted 28 November 2025

exceptional properties of $Fe_{32.6}Ni_{27.7}Co_{27.7}Ta_{5.0}Al_{7.0}$ alloy were attributed to the coherent, ordered nanoprecipitates dispersed homogeneously within a disordered FCC (A1) matrix [15], successfully overcoming the conventional strength–coercivity trade-off by minimizing magnetic pinning of domain walls [16]. Ye et al. developed the $Fe_{40}Co_{30}Mn_{15}Al_{15}$ alloy with high M_s and T_c and low coercivity (H_c). The microstructure comprised an ordered B2-phase matrix enriched with Co and Al and uniformly distributed BCC nanoprecipitates enriched with Fe and Mn [17]. Further work on the $AlCo_xCr_{1-x}FeNi$ system showed that M_s, H_c, and T_c could be significantly modified by varying Co and Cr content, resulting in either soft or hard magnetic properties depending on the nature of spinodal decomposition within BCC grains [18]. Recently, Gong et al. designed $Fe_{60}Cr_{18}Al_{13}Ni_8Mn_{0.9}Cu_{0.3}$ and $Fe_{57}Cr_{17}Al_{18}Ni_7Mn_1Cu_{0.3}$ alloys with excellent multifunctional properties due to the coexistence of a disordered BCC matrix and ordered B2 precipitates [19].

Most Alnico alloys exhibit isotropic properties in their as-cast state, characterized by random grain orientation [20]. To induce preferential magnetic alignment and develop anisotropic properties, these alloys undergo thermomagnetic treatment. This process involves heating above a critical temperature followed by cooling within an externally applied magnetic field [21–25], which is essential for optimizing their magnetic properties. Without this treatment, Alnico alloys exhibit a low H_c of approximately 10 Oe, comparable to soft magnetic materials [26]. The heat treatment transforms Alnico into a mixture of Fe and Co-rich precipitates dispersed within a Ni and Al-rich matrix. The enhanced properties of Alnico 8 were attributed to the spinodal decomposition structure formed under specific thermal conditions [21]. This decomposition involves the high-temperature separation of the BCC phase into a ferromagnetic Fe-Co-rich phase and a paramagnetic Al-Ni-rich phase [22,25,27]. Consequently, the magnetic properties of Alnico alloys can be engineered to exhibit either soft or hard magnetic behavior through controlled alloying with elements like Fe or Cu, enabling precise tuning of H_c and M_s [28].

The vast compositional space and design flexibility of HEAs present extensive opportunities to exploit complex phase transformations, such as spinodal decomposition [29,30]. This has motivated recent studies on the effects of adding elements in equimolar or near-equimolar amounts on the magnetic properties of Alnico-based HEAs [31–36]. In contrast to the complex thermal treatments required for conventional Alnico alloys, the $Fe_2CoNiAlCu_{0.4}Ti_{0.4}$ alloy exhibited hard magnetic properties as an isotropic cast magnet [34]. The origin of this hard magnetism was attributed to the hierarchically heterogeneous nanostructure, consisting of alternately distributed, anisotropic Fe-rich and Fe-lean nanoarrays within coherent $L2_1$ nanocells and A2 cell boundaries [31]. Furthermore, the hard magnetic properties of this alloy were enhanced following magnetic annealing.

Compared to other computational approaches, such as density functional theory-based magnetic predictions [37–39], spin dynamics Monte Carlo simulations [40,41], and machine learning models [42,43], the high-throughput CALPHAD method offers a unique balance of scalability, thermodynamic consistency, and direct relevance to alloy design. While first-principles and molecular dynamics methods provide high accuracy at the atomic scale, their substantial computational cost limits their applicability for large-scale compositional screening [44]. As reviewed by Mooraj et al., CALPHAD-based workflows enable rapid and reliable predictions of phase formation and transformation temperatures across broad compositional spaces [45].

To investigate the vast unexplored compositional and microstructural potential of HEAs, the implementation of high-throughput computational methods is essential for accelerating the discovery process. For instance, Zeng et al. integrated high-throughput CALPHAD with machine learning and experiments to discover novel eutectic HEAs [46], while Feng et al. employed it to design HEAs for high-temperature applications [47]. Recently, this technique has been used to develop a new Al-based multicomponent alloy from post-consumer scrap [48], and to discover eutectic HEAs that exhibit high hardness and compatibility with rapid solidification processes [49].

Although these studies demonstrate the potential of high-throughput CALPHAD for alloy discovery, its application in optimizing targeted functional properties remains limited. Notably, this approach has not yet been applied to the discovery and optimization of magnetic alloys. The present work addresses this gap by employing high-throughput CALPHAD simulations to optimize phase stability and guide the design of magnetic HEAs.

Motivated by these opportunities, this study aims to develop an integrated framework that combines high-throughput CALPHAD calculations with statistical data analysis to accelerate the discovery of novel magnetic HEAs. By leveraging the strengths of integrated computational materials engineering and advanced manufacturing techniques, such as spark plasma sintering (SPS), we seek to establish a new paradigm for rapid, cost-effective development of magnetic materials, and to elucidate key microstructure-property relationships critical for sustainable magnet design. Alnico 5 was selected as the benchmark since it is a commercially established, rare-earth-free magnet with a compositional basis like the HEA investigated. This provides a direct comparison of magnetic performance and microstructural evolution under identical processing conditions, offering a relevant context for evaluating the HEA as a potential sustainable alternative.

2. Experimental

2.1. High-throughput CALPHAD calculations

A schematic diagram for identifying magnetic HEAs is shown in Fig. 1. The design strategy follows the key steps typically employed in high-throughput CALPHAD calculations [50].

The initial step involved defining an elemental palette based on the standard compositions of various Alnico alloys and potential Fe-Co-Ni-Al-Cu-Ti-based HEAs. Literature data were collected to create a palette of elements, including elemental compositions and corresponding magnetic properties. The Fe–Co–Ni–Al–Cu–Ti system was selected since Fe, Co, and Ni provide strong ferromagnetic contributions [25,26]. Al and Ti act as ordering elements that stabilize intermetallic phases, while Cu tends to segregate and promote spinodal decomposition [20,51–53].

Expensive or scarce elements such as rare-earth elements, Ta, and Nb were avoided despite their reported beneficial effects [15,21,54]. Mn

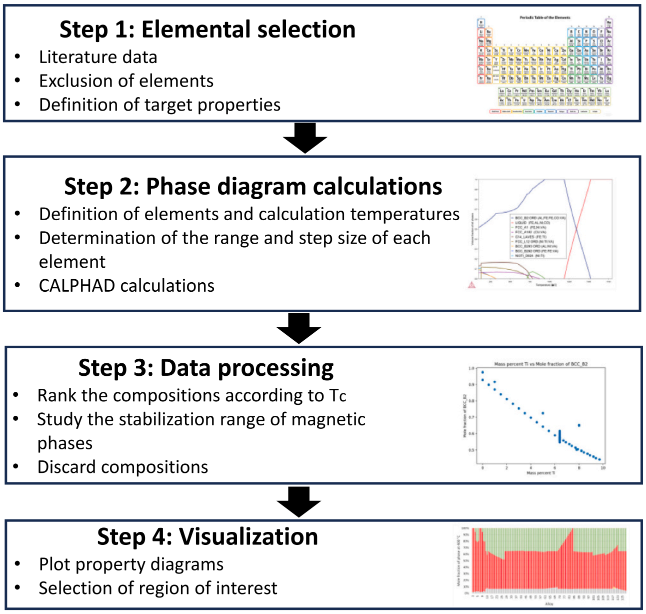

Fig. 1. Alloy design strategy for identifying magnetic HEAs.

was also excluded, as CoCrFeCuNi exhibited a superior M_s compared to CoCrFeMnNi [13]. The second step involved creating a composition list and performing phase diagram calculations. The compositional ranges and incremental step sizes for each element used in the high-throughput CALPHAD calculations are listed in Table 1.

This study examined 128 alloy compositions, including 114 newly designed systems and 14 benchmark alloys (Table 2). To evaluate phase stability and magnetic properties, high-throughput CALPHAD simulations were conducted using Thermo-Calc (Thermo-Calc Software AB, Stockholm, Sweden) [55] with the TCHEA7 database. These simulations provided temperature-dependent predictions of T_c, phase fractions, and phase compositions.

The calculated results for all 128 compositions, including the BCC_B2 phase fraction and T_c at key temperatures, were extracted and compiled into a structured dataset for analysis. Data visualization and statistical filtering were performed using the Julius AI data analysis tool (Caesar Labs, Inc., San Francisco, USA) to identify optimal composition ranges.

An optimal subset was then identified by performing a Boolean intersection of the compositions that simultaneously exceeded both thresholds. This subset, representing the top 25 % of compositions exhibiting concurrent enhancement in BCC_B2 phase stability and T_c, was considered statistically representative of the most promising region of the design space.

Finally, the mass fractions of Fe, Co, Ni, Al, Cu, and Ti within this optimal subset were analyzed. Their statistical distributions were used to establish robust composition windows correlated with high performance. A single composition was subsequently selected from this subset as the candidate that best matched the defined criteria.

2.2. Manufacturing

The $Fe_{42}Co_{17}Ni_{12}Al_{17}Cu_6Ti_6$ HEA was prepared by SPS using elemental powders of Fe, Co, Ni, Al, Cu, and Ti with particle size of $\leq$ 50 μm and a purity of $\geq$ 99.7 wt% (Nanoval GmbH, Berlin, Germany). The target and chemical compositions of the initial powders are summarized in Table 3, while the SPS processing conditions are detailed in Table 4. Sintering was carried out in an SPS furnace model S8451 (FCT Systeme, Frankenblick, Germany) under a vacuum of 4 mbar and with uniaxial pressure of 50 MPa. The alloy powders were loaded into a graphite die, with boron nitride applied to the punches and graphite foil inserted between the die wall and the powder. This configuration ensured uniform densification and prevented contamination or sticking during sintering.

Temperature control was achieved using a pyrometer positioned to measure the temperature inside the graphite punch. The temperature was increased to the target sintering temperature (973–1273 K) at a heating rate of 80 $K\cdot min^{-1}$, and held for 120 s. After sintering, the graphite spacers, pressing tools, and samples were cooled to room temperature by circulating water through the electrodes. The resulting cylindrical samples were 18 mm in diameter and 5.5 mm in height.

A benchmark Alnico 5 alloy was synthesized under identical SPS conditions at 1273 K, using commercially available FLNG34 powder (Yuxiang Magnetic Materials, Xiamen, China) to ensure a direct comparison of their as-sintered microstructures and magnetic properties.

Table 1
Compositional ranges and step sizes used in the high-throughput CALPHAD calculations.

Element (wt %)	Fe	Co	Ni	Al	Cu	Ti
Range	Bal.	3.6–38.0	9.5–24.1	3.5–11.0	3.0 – 11.3	0.0 – 9.7
Step size	Bal.	1.0	1.0	0.5	0.5	0.5

2.3. Microstructural characterization

The initial powders and powder mixture were characterized using a field emission scanning electron microscope (FE-SEM), equipped with an energy-dispersive X-ray spectrometry (EDS) model JSM-IT700HR (Jeol, Croissy-sur-Seine, France). Microstructural characterization and hardness test specimens were sectioned from the sintered samples and prepared according to standard metallographic procedures, including hot mounting in conductive resin, grinding, and polishing.

The microstructure and local chemical composition of each region were further analyzed by FE-SEM and EDS. Grain size and porosity were quantitatively determined using ImageJ software (University of Wisconsin-Madison, Madison, USA). For each sintering condition, at least five randomly selected SEM images (129.1 μm × 96.7 μm) were analyzed, and a minimum of 100 grains were measured to ensure statistical reliability. X-ray diffraction (XRD) analysis was conducted using a model D8 Advance diffractometer (Bruker, Karlsruhe, Germany) with Cu Kα radiation operated at 40 kV and 40 mA. Diffraction patterns were collected from 15° to 90° (2θ) range with a step size of 0.03°, at a dwell time of 1.0 s/step. The powder diffraction file (PDF) database 2008 was used for phase identification.

Fig. 2 shows the morphology and elemental distribution of the atomized powders. As illustrated in Fig. 2(a), the powder particles are predominantly spherical, while satellite particles are occasionally observed adhering to larger ones (Fig. 2(b)). The backscattered FE-SEM image and corresponding EDS maps in Fig. 2(c) confirm a uniform distribution of all constituent elements within the powder particles.

2.4. Mechanical and magnetic properties

The Vickers hardness was measured using a FV-700 model (Future-Tech, Kawasaki, Japan) system on the polished sample surface, with a 1 kg load according to ISO 6507–1.0 standard. The density was determined using the Archimedes method.

The magnetic properties of the samples sintered at different temperatures and the manufactured Alnico 5 benchmark, including intrinsic coercivity (H_{cj}), H_c, remanence (B_r) and maximum energy product (BH_{max}), were assessed at room temperature using a Permagraph (Magnet-Physik, Cologne, Germany). The static peak magnetic flux density (B) of the samples at 853 K, 873 K, 923 K, 973 K and 1033 K and a commercial Alnico 5, (Supermagnete, Uster, Switzerland) was measured using a Gaussmeter model GM05 (Hirst, Falmouth, United Kingdom). The experimental T_c was identified as the temperature at which the measured B became negligible.

3. Results and discussion

3.1. High-throughput CALPHAD calculations and statistical data analysis

To design a novel HEA, the primary objectives were to maximize the volume fraction of magnetic phases and to achieve a T_c comparable to that of the benchmark alloys in Table 2 (Alloys 1 – 14). Given the strong temperature dependence of phase formation and magnetic properties, four representative temperatures, ranging from 473 K to 1273 K, were selected to evaluate phase stability across a broad thermal spectrum. This range was chosen to capture key transformation regimes in magnetic alloys, including ordering, spinodal decomposition, and isothermal annealing, which are essential for shaping the final microstructure.

Fig. 3 presents the high-throughput screening results of the equilibrium phases at 1273 K, revealing two distinct compositional regions defined by their dominant phases. Region 1 (Alloys 1 – 70) is characterized by a disordered state, where the ideal atomic ordering required for the magnetically favorable BCC_B2 phase is not fully established. In this region, Thermo-Calc predicts a non-ideal variant, designated as BCC_B2#2, with a representative formula unit of (Al,Fe,Co,Ni:Co,Ni,Fe,Al:VA). This indicates partial atomic disorder across the sublattices: Al,

Table 2
Chemical composition (wt%) of the simulated benchmark alloys.

Alloy	Name	Fe	Co	Ni	Al	Cu	Ti	Type
1	Alnico 2	55.0	13.0	19.0	10.0	3.0	0.0	Isotropic cast
2	Alnico 5	51.0	24.0	14.0	8.0	3.0	0.0	Anisotropic cast
3	Alnico 6	48.0	24.0	16.0	8.0	3.0	1.0	
4	Alnico 8	34.0	35.0	15.0	7.0	4.0	5.0	
5	Alnico 8 HC	29.0	38.0	14.0	8.0	3.0	8.0	
6	Alnico 9	34.0	35.0	15.0	7.0	4.0	5.0	
7	Alnico 2	55.0	13.0	19.0	10.0	3.0	0.0	Isotropic sintered
8	Alnico 5	51.0	24.0	14.0	8.0	3.0	0.0	Anisotropic sintered
9	Alnico 6	49.0	24.0	15.0	8.0	3.0	1.0	
10	Alnico 8	34.0	35.0	15.0	7.0	4.0	5.0	
11	Alnico 8 HC	30.0	38.0	14.0	7.0	3.0	8.0	
12	$Fe_2CoNiAlCu_xTi_x$	37.1	19.6	19.5	9.0	8.4	6.4	Cast [34]
13	$Fe_2CoNiAlCu_xTi_x$	22.7	24.1	24.0	11.0	10.4	7.8	Cast [34]
14	$Fe_2CoNiAlCu_{0.4}Ti_{0.4}$	37.0	19.6	19.5	9.0	8.5	6.4	Cast [31]

Table 3
Target and experimental compositions of the initial powder.

Powder	Fe	Co	Ni	Al	Cu	Ti
Target (wt%)	43	20	14	9	8	6
Target (at%)	42	17	12	17	6	6
Experimental (wt%)	45.0 ± 0.2	19.1 ± 0.2	11.8 ± 0.2	9.5 ± 0.1	7.6 ± 0.1	7.0 ± 0.1
Experimental (at%)	41.4 ± 0.2	16.6 ± 0.1	10.3 ± 0.1	18.0 ± 0.1	6.1 ± 0.1	7.5 ± 0.1

Table 4
A summary of SPS manufacturing conditions.

Sintering temperature	973 K, 1073 K, 1173 K and 1273 K
Holding time	120 – 300 s
Pressure	50 MPa
Mold	graphite
Plungers	graphite
Samples	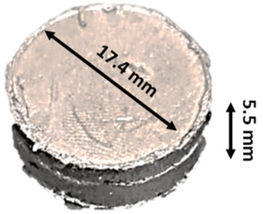

Fe, Co, and Ni can occupy sublattice 1; Co, Ni, Fe, and Al can occupy sublattice 2; and vacancies (VA) reside on sublattice 3. The persistence of the disordered BCC_B2#2 phase at 1273 K suggests that the ordering transformation remains incomplete.

In contrast, Region 2 (Alloys 71 – 128) is dominated by the fully ordered BCC_B2 phase, characterized by the ideal formula unit (Ni,Co: Al,Fe:VA). This confirms the successful formation of the magnetically desirable, ordered structure at 1273 K. A subrange within this region (Alloys 115–120), characterized by Al contents below 6 wt%, is predominantly composed of a disordered FCC_L12#2 phase (Fe,Co,Ni,Al: Fe,Co,Ni:VA), which is absent in the benchmark alloys (Alloys 1–9 and 14). Particularly, the FCC_L12 (Cu:Cu:VA) phase was related to the degradation of H_c and M_s after magnetic annealing in the $Fe_2CoNiAlCu_{0.4}Ti_{0.4}$ HEA [31].

Fig. 4 presents the high-throughput screening of equilibrium phases at 873 K, a temperature selected for its relevance to the 823–923 K range typically employed for magnetic annealing in permanent magnets. This thermal treatment promotes atomic ordering, a process critical for establishing the optimal crystal symmetry and magnetic domain alignment necessary for high coercivity. The results confirm the formation of the ordered BCC_B2 phase across all investigated alloys, underscoring its exceptional stability under these conditions. This is a promising finding, as the BCC_B2 phase is a key contributor to high magnetic performance.

The benchmark Alnico alloys (Alloys 1–11) exhibit a dual-phase microstructure at 873 K, consisting of both the disordered BCC_B2#2 and the ordered BCC_B2 phases. To optimize magnetic properties, compositions with a minimized fraction of the disordered phase should be prioritized, as its presence is known to degrade magnetic properties. Notably, the phase stability at 873 K also facilitates the formation of significant amounts of the HEUSLER_L21 (Ti:Al:Ni) phase. However, this phase is absent in certain benchmark alloys and in a subset of the potential compositions (Alloys 82–84 and 101–110).

Fig. 5(a) presents the equilibrium phases at 673 K, as determined by high-throughput screening. At this temperature, the fully ordered BCC_B2 phase is predominant across all alloy compositions, followed by the HEUSLER_L21 and FCC_L12 phases. Notably, the HEUSLER_L21 phase is absent in benchmark Alnico 2 and 5, as well as in Alloy 84.

With a further decrease in temperature to 473 K (Fig. 5b), BCC_B2 remains the dominant phase, but the volume fractions of the HEUSLER_L21 and FCC_L12 phases increase. A key observation at this temperature is the formation of the FCC_L12 phase in the Alnico alloys, where it was not present at 673 K. This temperature-dependent phase evolution underscores the critical influence of thermal history on phase stability and atomic ordering, providing essential insights for tailoring the heat treatment of these magnetic alloys.

Fig. 6 summarizes the T_c results from the high-throughput screening at 473 K, 673 K, and 873 K. For reference, the T_c range of commercial Alnico alloys (1023–1133 K) is shown, representing the lowest and highest reported values. Notably, most of the studied compositions exhibit T_c values within this commercial range. The results further reveal a strong positive correlation between T_c and the volume fraction of the magnetic BCC_B2 phase across all temperatures.

At 473 K (Fig. 6(a)), most calculated T_c values fall below the typical range for commercial Alnico alloys, including benchmark compositions. At 673 K (Fig. 6(b)), a synergistic interaction between Co and Ni is evident. Although T_c generally decreases with lower Ni content, a notable rebound occurs below 12.5 wt% Ni (Alloys 108–110), where T_c values approach the performance of commercial Alnico alloys. The highest T_c values at this temperature are observed in Alloys 111–121 (19.6 wt% Co, 19.5 wt% Ni, 8.5 wt% Cu, 6.4 wt% Ti), while Al content varies from 9.0 to 3.5 wt%. Within this group, a clear trend of increasing T_c with decreasing Al content is evident.

The trend at 873 K (Fig. 6(c)) further highlights the critical influence of composition, revealing that alloys with higher Ti content demonstrate superior T_c. This underscores the role of Ti in stabilizing high-T_c phases at elevated temperatures. Consistently, Alloys 111–121 again exhibit superior performance, outperforming other compositions. These results reaffirm that optimizing the Co:Ni ratio while reducing Al content is an effective strategy to maximize T_c without sacrificing phase stability.

To process the extensive dataset from high-throughput CALPHAD calculations, Thermo-Calc output files were systematically analyzed

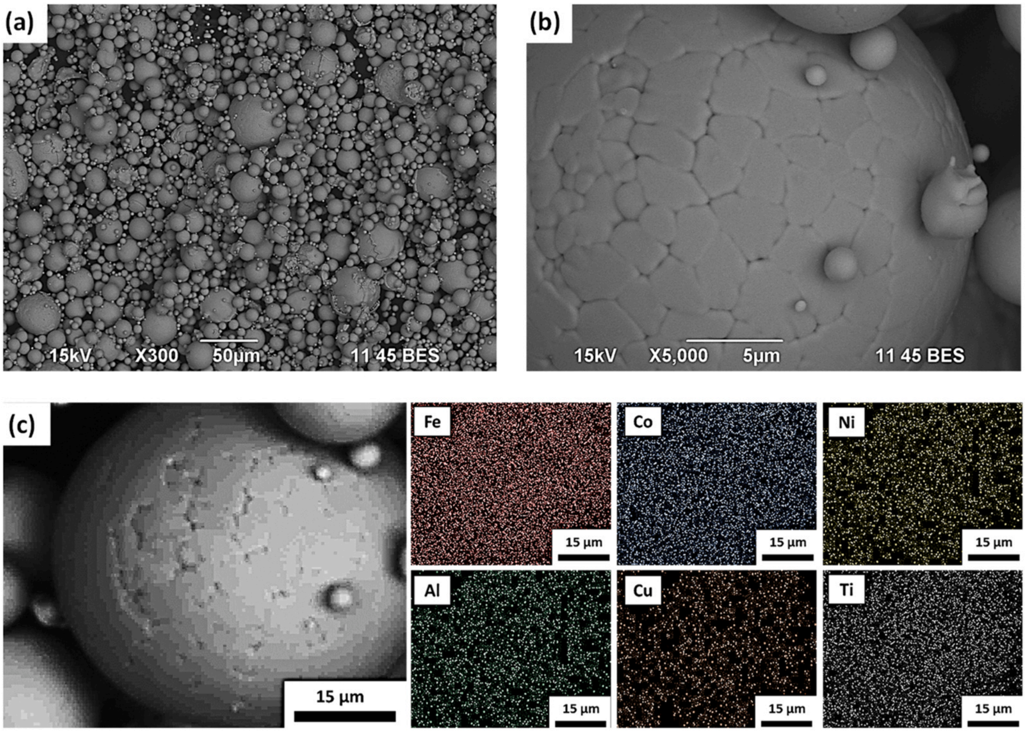

Fig. 2. Backscattered FE-SEM images of (a) granulated powder and (b) surface of the granules. (c) FE-SEM image and the corresponding EDS elemental maps of the initial powders.

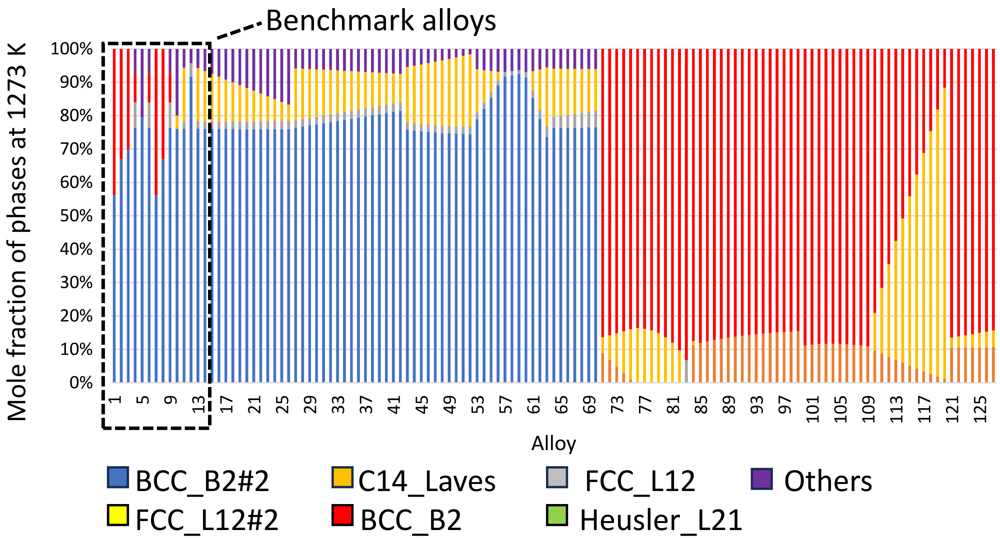

Fig. 3. High-throughput screening of equilibrium phases at 1273 K.

using statistical methods. The analysis identified the top 25 % of compositions for each target property using thresholds of 0.61 mol fraction for BCC_B2 formation, and 1102 K for T_c. Table 5 summarizes the optimal composition ranges from these samples and the final target alloy.

The selected composition represents a balance of multiple design criteria. A target Fe content of 43 wt% was chosen to fall within the optimal range for BCC_B2 phase formation while approaching the upper limit for high T_c. To reduce reliance on strategic elements critical for battery technologies, the contents of Co and Ni were minimized. The Co content was set to 20 wt%, a value that lies within the stability window for the BCC_B2 phase and near the lower boundary of the high-T_c range yet remains sufficient to ensure robust magnetic performance. The Ni content was set at 14 wt%, just above the threshold for BCC_B2 formation but slightly below its optimal T_c range, representing a calculated compromise. An Al content of 9 wt% was selected as it resides comfortably within the stability windows for both BCC_B2 formation and high T_c. Similarly, the Cu content of 8 wt% aligns well with the optimal ranges for both criteria. Finally, the Ti content was fixed at 6 wt % to optimally balance the two primary CALPHAD-identified design targets: maximizing the BCC_B2 phase fraction and increasing T_c. As detailed in Table 5, a Ti content of 4 ± 3 wt% maximizes the BCC_B2 fraction, while 7 ± 1 wt% maximizes T_c. The selected composition of 6 wt% Ti represents the most favorable compromise, sustaining a high BCC_B2 fraction (Figs. 4 - 6) while achieving a near-optimal T_c (Fig. 6). This ensures a sufficient volume of the magnetic phase with excellent

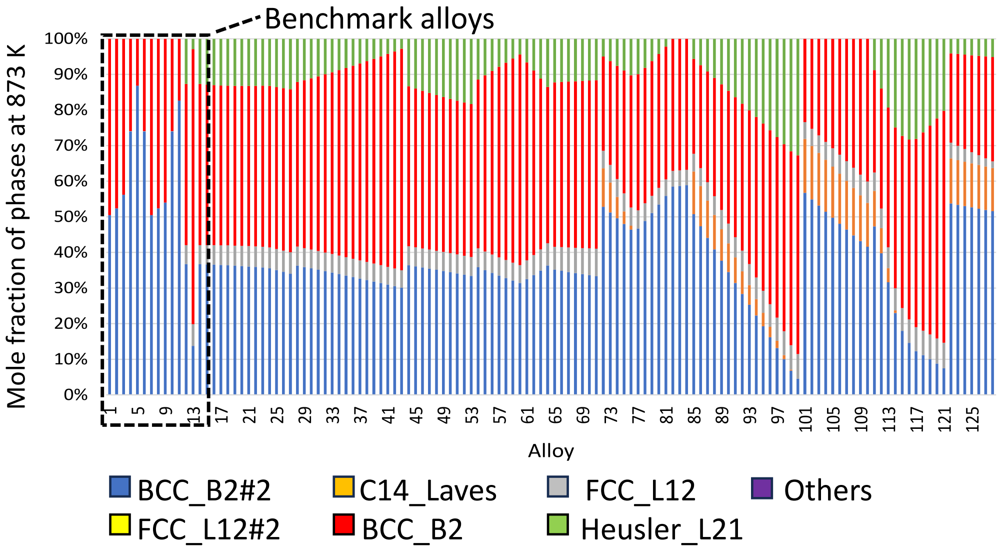

Fig. 4. High-throughput screening of equilibrium phases at 873 K.

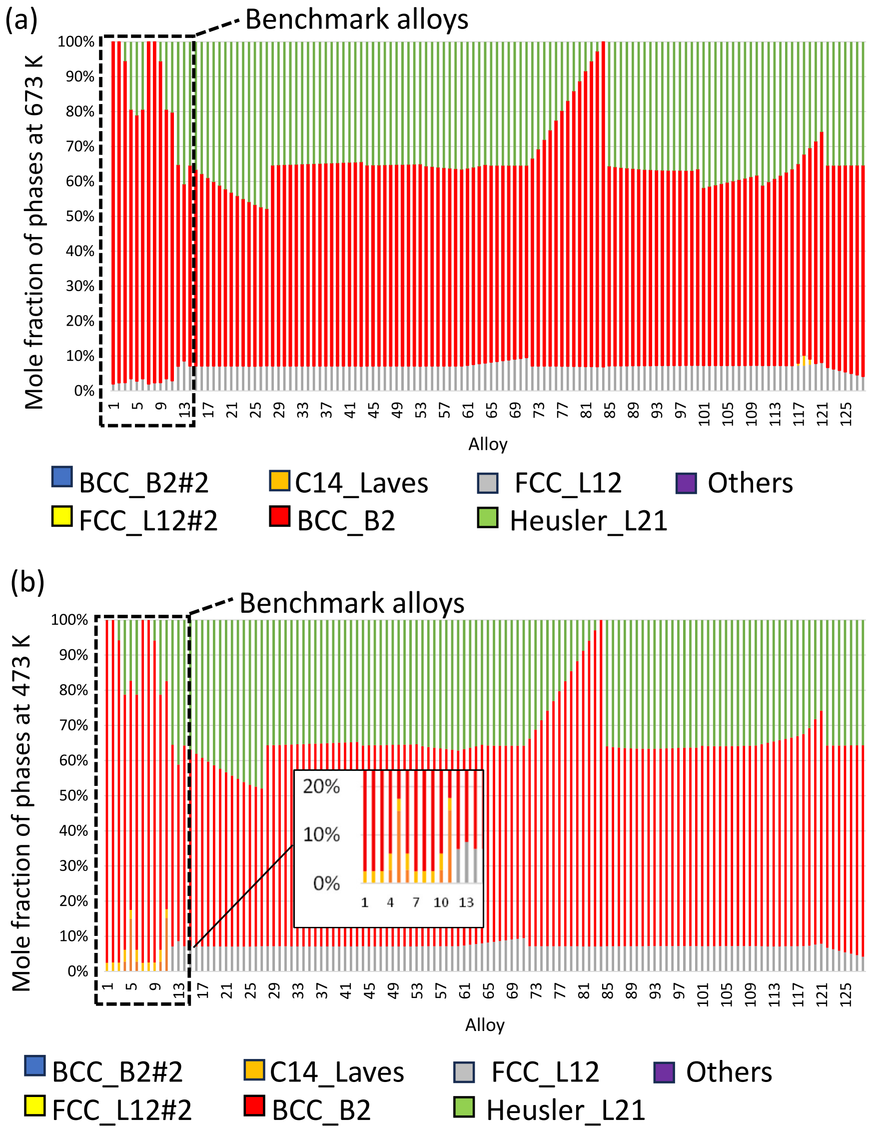

Fig. 5. High-throughput screening of equilibrium phases at (a) 673 K and (b) 473 K.

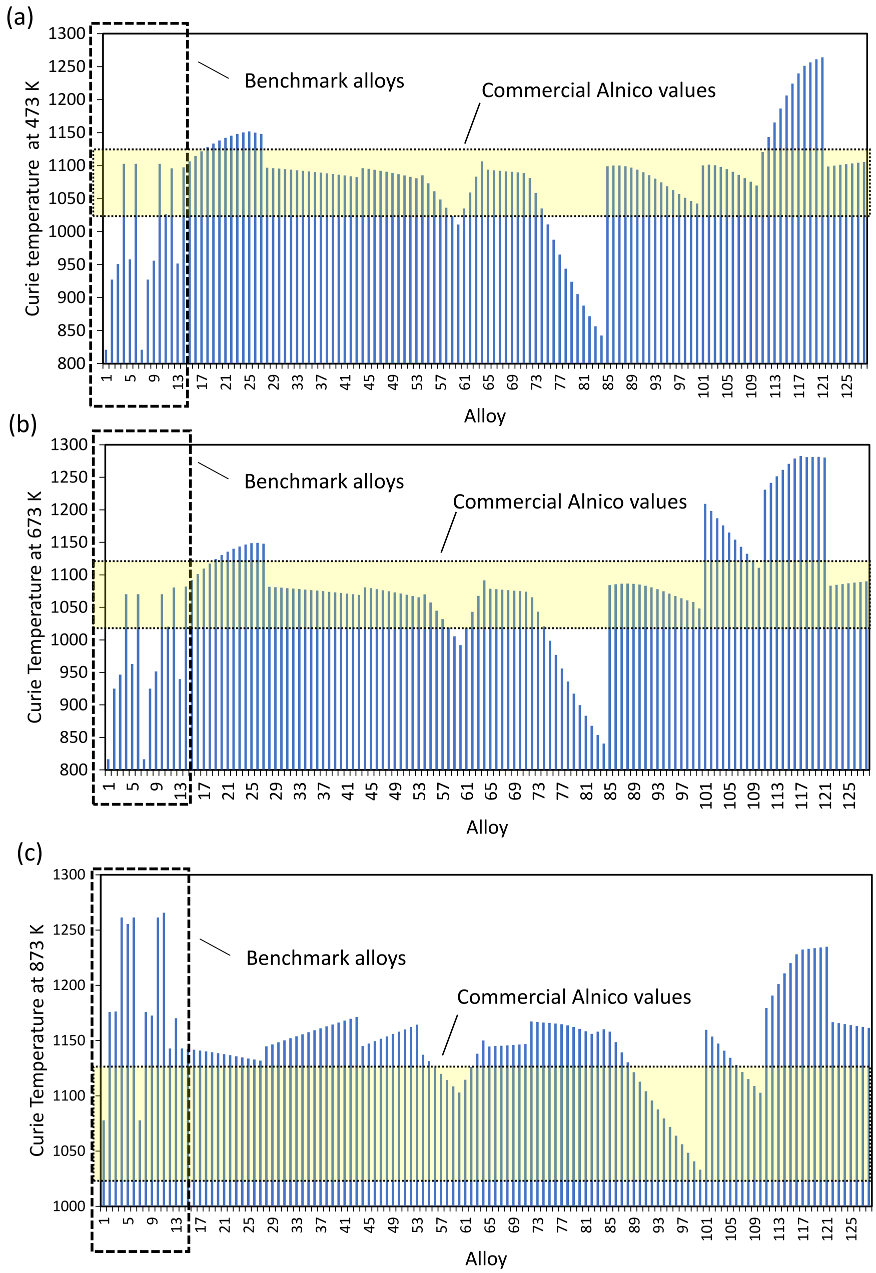

Fig. 6. High-throughput screening of T_c at (a) 473 K, (b) 673 K and (c) 873 K.

Table 5
The optimal composition ranges for BCC_B2 phase formation and for high T_c.

Element (wt%)	BCC_B2			High T_c			Target
	Optimal	Min.	Max.	Optimal	Min.	Max.	
Fe	42 ± 6	29	55	38 ± 3	34	43	43
Co	22 ± 6	13	38	21 ± 5	20	35	20
Ni	18 ± 2	14	19	19 ± 1	15	19	14
Al	8 ± 2	3	10	8 ± 2	3	9	9
Cu	6 ± 3	3	8	8 ± 2	4	9	8
Ti	4 ± 3	0	8	7 ± 1	5	10	6

thermal stability.

3.2. Phase formation rules for HEAs

Based on the Hume-Rothery rules, several empirical thermophysical parameters have been proposed as guidelines for predicting phase formation in HEAs [1,56,57]. These parameters include the ideal configurational entropy (ΔS_{conf}), mixing enthalpy (ΔH_{mix}), atomic size difference (δ), electronegativity difference ($\Delta\chi$), parameter Ω, and valence electron concentration (VEC).

The accepted criteria for the formation of a single-phase solid solution (SS) are: $\Delta S_{conf} > 1.5$ R, $-15 \leq \Delta H_{mix} \leq 5$ kJ/mol, $\delta \leq 6.6$ %, $\Delta\chi \leq 0.17$, and $\Omega \geq 1.1$. Regarding crystal structure stability, the FCC phase is stable when VEC ≥ 8, while the BCC phase is favored for VEC ≤ 6.87. A mixed FCC + BCC microstructure is typically expected for intermediate values ($6.87 <$ VEC< 8.00). The corresponding values were calculated using the following equations:

$$\Delta S_{mix} = \Delta S_{conf} = -R\sum_{i}^{n} X_i.\ln X_i \qquad (1)$$

$$\Delta H_{mix} = 4\sum_{i=1,i\neq j}^{n} C_i.C_j.\Delta H_{i-j}^{mix} \qquad (2)$$

$$\delta = 100\sqrt{\sum_{i=1}^{n} C_i\left(1-\frac{r_i}{\bar{r}}\right)^2} \qquad (3)$$

$$\Delta\chi = \sqrt{\sum_{i=1}^{n} C_i(\chi_i - \bar{\chi})^2} \qquad (4)$$

$$\Omega = \frac{\overline{T_m}.\Delta S_{mix}}{|\Delta H_{mix}|} \qquad (5)$$

$$VEC = \sum_{i=1}^{n} C_i \bullet VEC_i \qquad (6)$$

where R is the gas constant (8.314 J. (mol.K)$^{-1}$); X_i is the atomic fraction of element i and n is the number of elements in the alloy; C_i is the atomic ratio of the ith element; C_j is the atomic ratio of the jth element; ΔH_{i-j}^{mix} is the enthalpy of mixing between ith and jth elements calculated by Miedema's model; r_i is the atomic radius of ith element; $\bar{r}$ is the composition weighted average atomic radius; χ_i is the Pauling electronegativity for the ith component and $\bar{\chi}$ is the composition weighted average electronegativity of all the components, $\overline{T_m}$ is the average melting point of the elements in the alloy and VEC_i is the valence electron concentration of element i.

According to the results summarized in Table 6, the $Fe_{42}Co_{17}Ni_{12}Al_{17}Cu_6Ti_6$ HEA exhibits a favorable combination of thermophysical parameters indicative of SS microstructure formation, likely consisting of a mixture of SS phases. This is consistent with the stability predicted by the VEC criterion, which indicates a mixed FCC and BCC microstructure for values in the range of $6.9 \leq$ VEC < 8 [58]. A closer analysis reveals that both the δ and the Ω parameter approach their respective thresholds for SS formation. This proximity suggests that while SS formation is thermodynamically favored, the stability of these phases may be sensitive to processing conditions.

3.3. *Microstructural characterization*

Fig. 7 presents FE-SEM images of the $Fe_{42}Co_{17}Ni_{12}Al_{17}Cu_6Ti_6$ HEA microstructure sintered at different temperatures. The analysis reveals a uniform, equiaxed granular morphology across all conditions, with no evidence of dendritic solidification. This indicates that the SPS process promoted solid-state formation without dendritic growth, resulting in a homogeneous microstructure [36]. This consistency suggests that sintering temperature is the primary factor controlling microstructural evolution in this system.

Table 6
Calculated thermo-physical parameters for the experimental $Fe_{41}Co_{17}Ni_{10}Al_{18}Cu_6Ti_7$ HEA.

ΔS_{mix} (J/mol • K)	ΔH_{mix} (kJ/mol)	δ (%)	Ω	Δχ	VEC
1.6 R	- 9.0	6.21	2.31	0.113	7.3

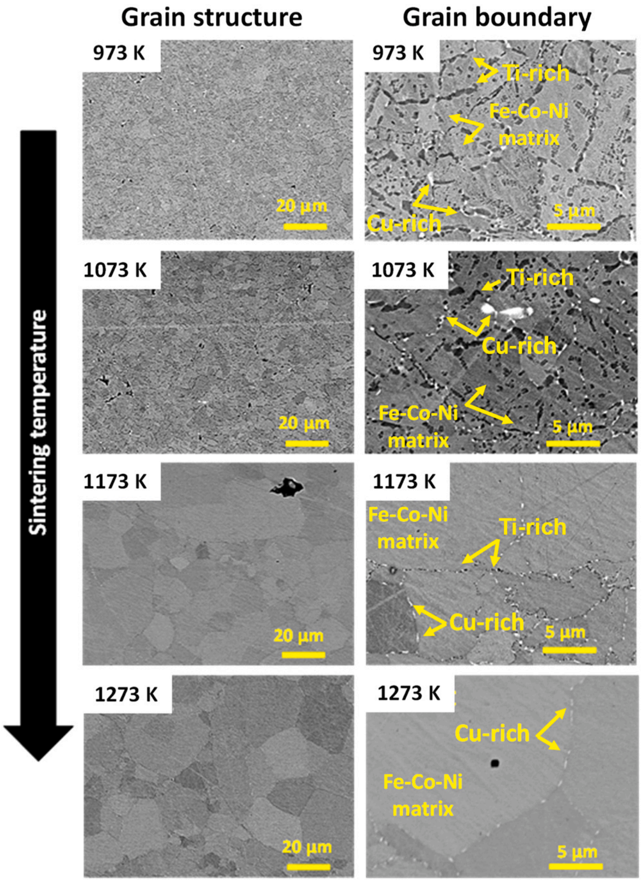

Fig. 7. Backscattered FE-SEM images of the $Fe_{42}Co_{17}Ni_{12}Al_{17}Cu_6Ti_6$ HEA sintered at 973 K, 1073 K, 1173 K, and 1273 K, illustrating the microstructural and phase evolution of the Fe-Co-Ni matrix (BCC_B2), Cu-rich (FCC_L12) and Ti-rich (HEUSLER_L21) phases.

As the sintering temperature increases, porosity is systematically reduced from 0.9 % to 0.6 %, then to 0.5 %, and finally 0.1 %, while simultaneously promoting grain coarsening, with the average equivalent grain diameter increasing from 19.8 ± 2.8 µm to 21.4 ± 5.1 µm, then to 31.2 ± 4.0 µm, and finally 48.8 ± 10.8 µm. The increased variability in grain size at 1273 K indicates irregular grain growth, which may affect magnetic performance given the strong dependence of magnetic properties on grain size [59–62].

These observations highlight a direct trade-off between density and grain size, emphasizing the need for careful optimization of the sintering temperature. Grain boundary analysis further reveals a temperature-dependent microstructural evolution. At 973–1073 K, coarse intermetallic compounds (ICs) with distinct dark and bright contrasts form are observed, while at 1173–1273 K, finer ICs precipitate along the grain boundaries.

Fig. 8 presents EDS mapping of the alloy sintered at 973 K, revealing distinct microstructural features that correspond to the contrasting grain boundary regions observed in Fig. 7. The elemental maps show good solubility of Fe, Co, Ni, and Al within the matrix, whereas Cu and Ti exhibit limited solubility and pronounced segregation. Specifically, Cu segregates at grain boundaries, which accounts for the light-contrast regions in the SEM images. This finding is consistent with previous reports on Alnico alloys, where Cu remains uniformly distributed in the matrix of Alnico 5 and 7 but segregates to grain boundaries in Ti-containing grades like Alnico 8 and 9 [20,25,51].

The limited solubility of Ti in the matrix also leads to its segregation, where it combines with Al and Ni to form distinctive rod-shaped precipitates exhibiting dark contrast. These features correspond to the

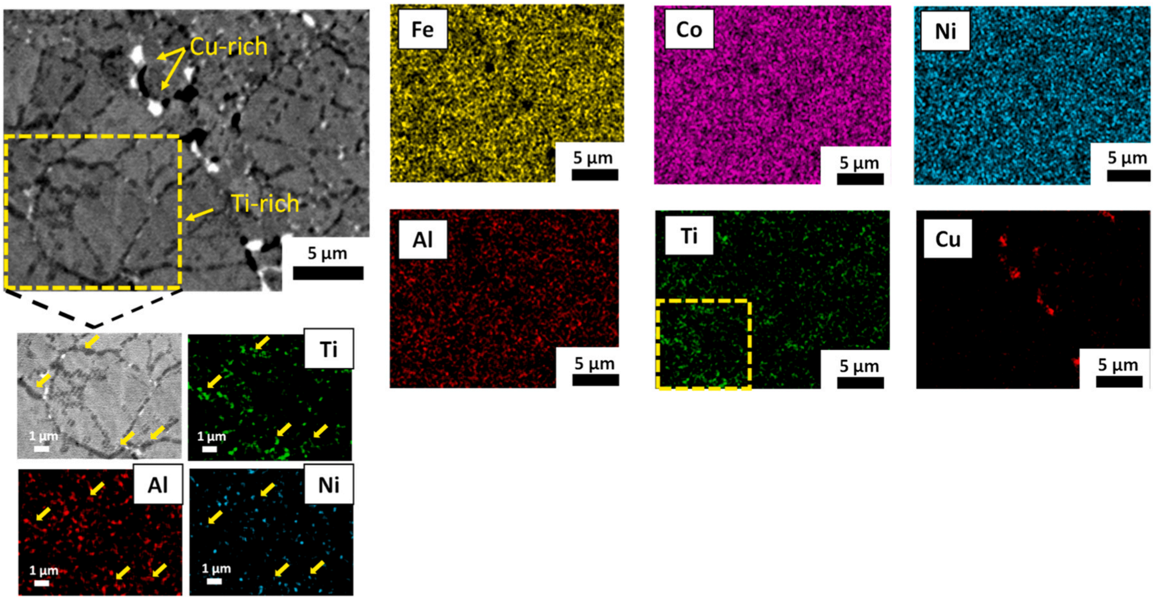

Fig. 8. FE-SEM image and elemental mapping of the grain boundaries in the $Fe_{42}Co_{17}Ni_{12}Al_{17}Cu_6Ti_6$ HEA sintered at 973 K.

Heusler phase with an $L2_1$ crystal structure, consistent with prior studies [52,53]. This is further supported by our equilibrium phase calculations, which predict the formation of HEUSLER_L21 (Ti:Al:Ni) phase (Figs. 4–5).

Fig. 9 shows the elemental distribution in the alloy sintered at 1073 K, revealing segregation patterns consistent with those observed at 973 K. The primary microstructural changes associated with the higher sintering temperature include significant grain coarsening and a more pronounced spatial separation between the Cu-rich and Ti-rich phases.

The FE-SEM and EDS analysis presented in Fig. 10 demonstrates significant grain growth due to sintering at 1173 K. The distributions of Fe, Co, Ni, and Al remain homogeneous throughout the matrix. Notably, fine Cu-rich and Ti-rich segregations are observed along the grain boundaries, which are significantly finer than those in microstructures formed at lower sintering temperatures.

Fig. 11 demonstrates that increasing the sintering temperature induces a near-linear grain coarsening, alongside a reduction in the size of ICs. While Fe, Co, Ni, and Al exhibit strong solubility within the supersaturated SS matrix, localized Cu-rich segregation persists.

XRD analysis was performed to identify the crystallographic phases in the as-sintered $Fe_{42}Co_{17}Ni_{12}Al_{17}Cu_6Ti_6$ HEA sintered at 1173 K and 1273 K. As shown in Fig. 12, the diffraction patterns indicate that the alloy consists predominantly of a BCC matrix with a minor FCC phase. The BCC phase is attributed to the supersaturated SS matrix, while the FCC phase is associated with Cu-rich segregation at grain boundaries, a feature consistent with observations in commercial Alnico magnets [63].

These findings are supported by equilibrium calculations in Fig. 5, which also predict the coexistence of BCC_B2 and FCC_L12 phases. Notably, the sample sintered at 1173 K exhibits additional XRD peaks corresponding to the Heusler $L2_1$ phase. These results align with previously reported phase equilibria for similar alloy systems. For instance, Na et al. observed a primary α-phase (BCC) alongside secondary Cu-rich (FCC) phases [34], while Chen et al. identified a microstructure comprising α-A2 (disordered BCC), α-$L2_1$ (ordered Heusler), and FCC Cu-rich nanoparticle phases in $Fe_{42}Co_{17}Ni_{12}Al_{17}Cu_6Ti_6$ [31].

At sintering temperatures $\leq$ 1173 K, the strongly negative ΔH_{mix} between Ni - Ti and Al dominates the Gibbs free energy ($\Delta G \approx \Delta H_{mix} - T{\cdot}\Delta S$) [57,64]. This provides a strong driving force for atomic ordering, leading to the nucleation of the Heusler $L2_1$ phase. This nucleation occurs preferentially at grain boundaries, where reduced activation barriers facilitate heterogeneous nucleation [65–67]. At these temperatures, the thermal energy is sufficient to enable limited atomic diffusion but remains low enough to prevent entropy-driven destabilization of the ordered intermetallic phases.

In contrast, at 1273 K, the increased thermal energy elevates the contribution of the entropic term ($-T{\cdot}\Delta S$) in the Gibbs free energy. This term counteracts and surpasses the ordering drive from the negative

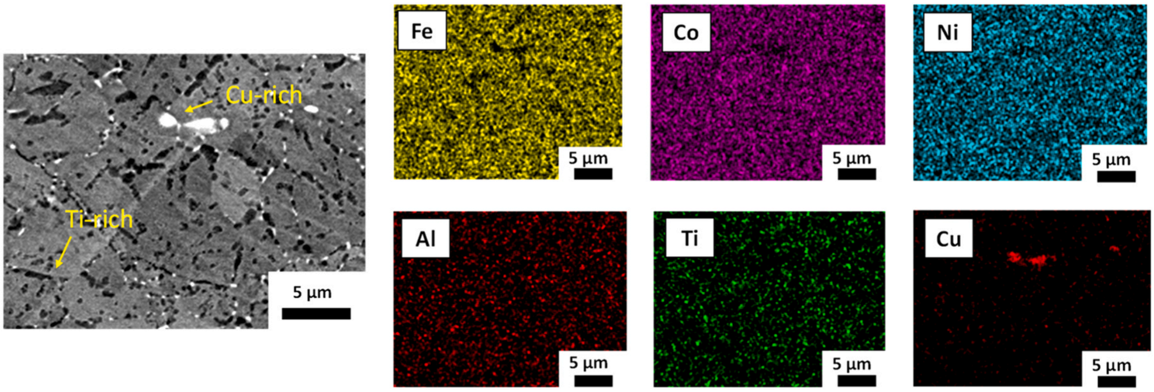

Fig. 9. FE-SEM image and elemental mapping of $Fe_{42}Co_{17}Ni_{12}Al_{17}Cu_6Ti_6$ HEA sintered at 1073 K.

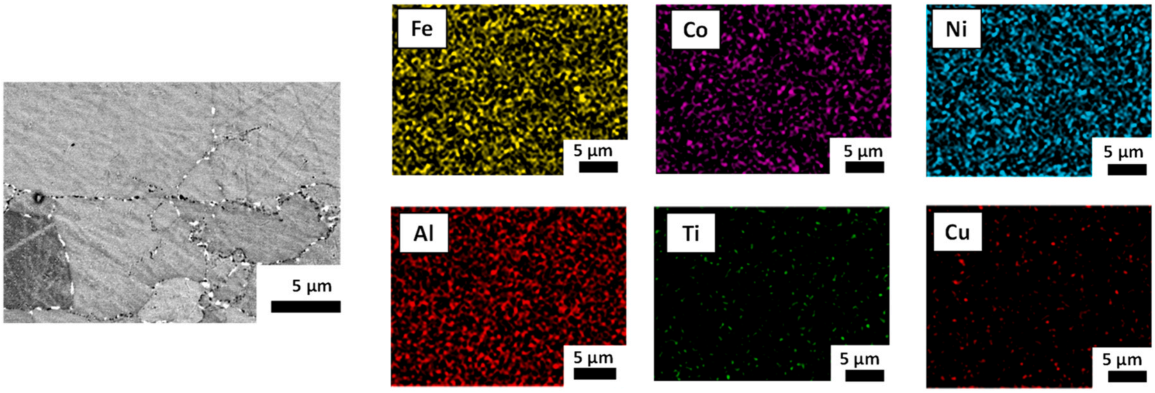

Fig. 10. FE-SEM image and elemental mapping of $Fe_{42}Co_{17}Ni_{12}Al_{17}Cu_6Ti_6$ HEA sintered at 1173 K.

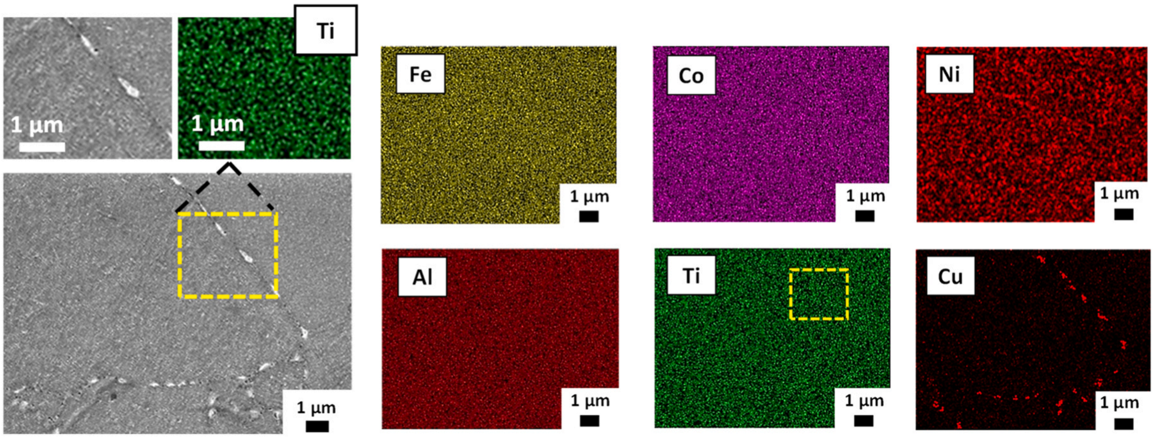

Fig. 11. FE-SEM image and elemental mapping of $Fe_{42}Co_{17}Ni_{12}Al_{17}Cu_6Ti_6$ HEA sintered at 1273 K.

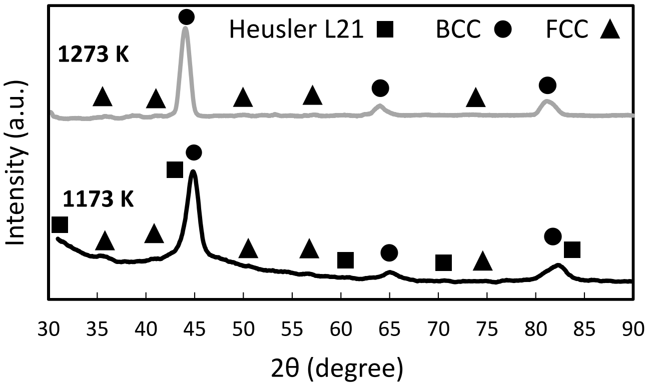

Fig. 12. XRD pattern of the as-sintered $Fe_{42}Co_{17}Ni_{12}Al_{17}Cu_6Ti_6$ HEA sintered at 1173 K and 1273 K.

ΔH_{mix}, resulting in the dissolution of the $L2_1$ phase into the BCC matrix. The cooling inherent to the SPS process then kinetically traps this metastable, dissolved state, effectively suppressing the reprecipitation of the $L2_1$ phase during cooling.

To benchmark the microstructural and magnetic properties of the $Fe_{42}Co_{17}Ni_{12}Al_{17}Cu_6Ti_6$ HEA, a reference Alnico 5 alloy was synthesized under identical processing conditions, including sintering at 1273 K. FE-SEM and EDS analyses in Fig. 13 reveal pronounced phase segregation in the as-sintered Alnico 5, with four distinct contrast regions indicating compositional variations. The primary SS matrix is rich in Fe, Co, and Ni, while secondary, lighter-contrast regions also contain these elements but in different ratios. Elemental mapping confirms the presence of rod-like, Ti-rich regions exhibiting dark contrast.

In contrast, Ti-rich features are observed only in $Fe_{42}Co_{17}Ni_{12}Al_{17}Cu_6Ti_6$ HEA sintered below 1273 K, highlighting a key difference in the temperature-dependent phase stability between the two alloys. However, both compositions exhibit Cu-rich segregation along grain boundaries, indicating a similar tendency for Cu partitioning during consolidation despite their differing overall chemistries.

3.4. Mechanical and magnetic properties

The theoretical density of $Fe_{42}Co_{17}Ni_{12}Al_{17}Cu_6Ti$ HEA, calculated using the rule of mixtures, is 7.2 g/cm^3 . The measured densities of the sintered samples were 7.0 g/cm^3 at 1173 K and 7.1 g/cm^3 at 1273 K. This indicates that a maximum relative density of 99 % of the theoretical value was achieved at 1273 K, indicating minor residual porosity.

The mean hardness was measured to be 707 ± 86 HV. Although hardness is not a primary functional property for magnetic materials, sufficient mechanical integrity is essential for applications such as motors, sensors, and actuators. The measured hardness falls within the typical range for Alnico alloys (500–700 HV), supporting its potential for such uses.

The magnetic properties were characterized using a permagraph system. The demagnetization curves in Fig. 14 exhibit a linear descent, which signifies constant permeability. This magnetic response is characteristic of soft magnetic materials.

As shown in Fig. 15, both the H_{cj} and BH_{max} increase with rising sintering temperature. This enhancement is primarily attributed to improved microstructural densification. The reduction in porosity from

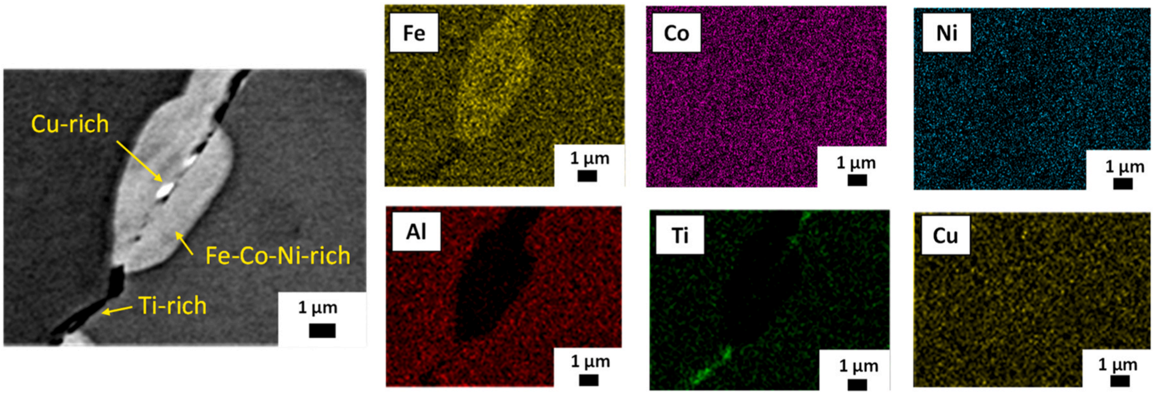

Fig. 13. FE-SEM image and elemental mapping of the benchmark Alnico 5 sintered at 1273 K.

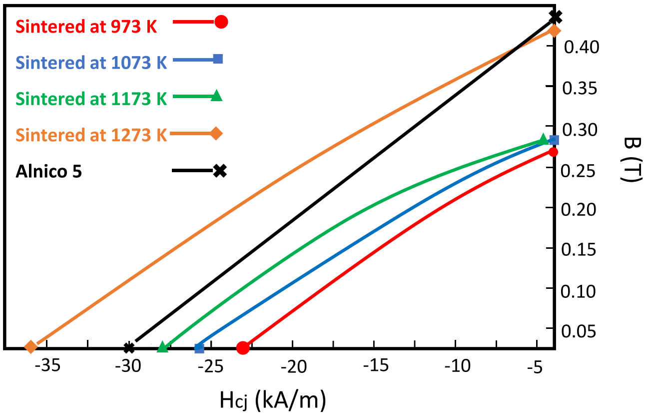

Fig. 14. Second quadrant of the hysteresis loop of $Fe_{42}Co_{17}Ni_{12}Al_{17}Cu_6Ti_6$ HEA sintered at different temperatures and benchmark Alnico 5 showing critical parameters.

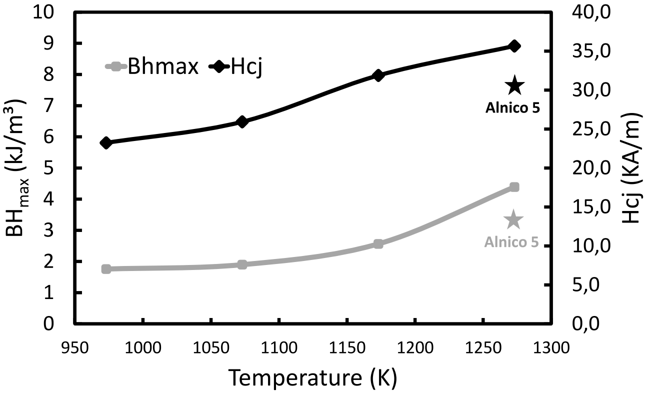

Fig. 15. The H_{cj} and BH_{max} of $Fe_{42}Co_{17}Ni_{12}Al_{17}Cu_6Ti_6$ HEA as a function of sintering temperature and benchmark Alnico 5 at 1273 K.

0.9 % to 0.1 % at the highest temperature minimizes the volume of pores, which otherwise disrupt the magnetic field and degrade performance [68,69].

The influence of sintering temperature on magnetic properties was evaluated by measuring the H_{cb} and B_r over the range of 973 K to 1273 K. As shown in Fig. 16, H_{cb} decreases slightly at lower temperatures before increasing markedly above 1073 K, reaching a maximum of 33.4 kA/m at 1273 K. This trend is attributed to enhanced densification and a corresponding reduction in porosity at higher sintering temperatures. Furthermore, the controlled grain growth observed in Fig. 7 promotes favorable magnetic domain alignment while avoiding the detrimental effects of excessive grain coarsening [70,71].

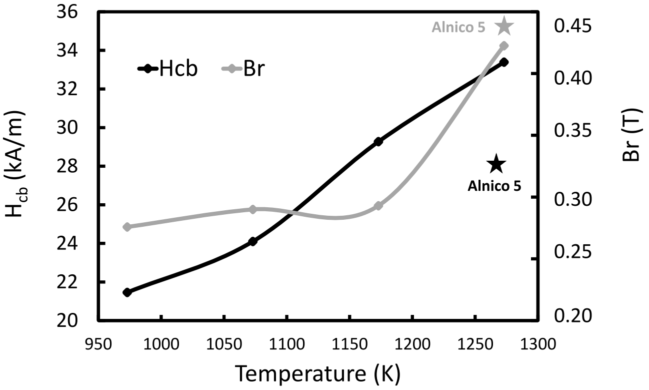

Fig. 16. The H_{cb} and B_r of $Fe_{42}Co_{17}Ni_{12}Al_{17}Cu_6Ti_6$ HEA as a function of sintering temperature and benchmark Alnico 5 at 1273 K.

Similarly, B_r remains stable at lower temperatures and increases substantially above 1073 K, peaking at 0.42 T at 1273 K. The simultaneous enhancement of both H_{cb} and B_r demonstrates that a sintering temperature of 1273 K is optimal for achieving the best magnetic performance in this alloy.

Fig. 17 compares the thermal stability of B for $Fe_{42}Co_{17}Ni_{12}Al_{17}Cu_6Ti_6$ HEA and the commercial Alnico 5 magnet. Alnico 5 exhibits high B retention up to approximately 870 K, beyond which it undergoes a steep decline, approaching zero near 970 K. In contrast, $Fe_{42}Co_{17}Ni_{12}Al_{17}Cu_6Ti_6$ HEA maintains a moderate remanence level up

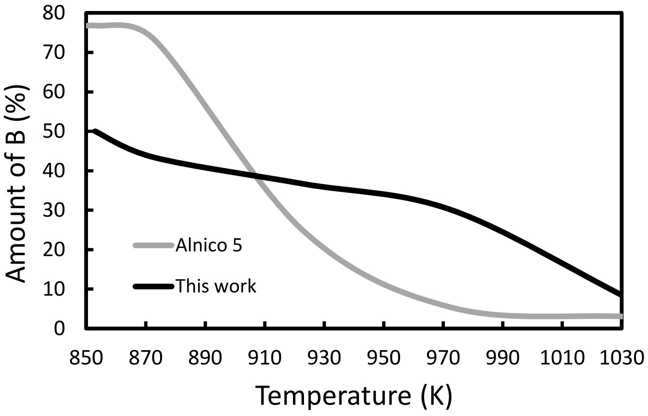

Fig. 17. Amount of B as a function of temperature.

to 950 K, with a more gradual loss profile, eventually reaching low values at 1030 K. This more progressive decline underscores the superior thermal stability inherent to 3d-transition metal-based HEAs [72].

Quantitatively, the HEA retains 50 %, 43 %, 37 %, and 30 % of its room-temperature B value at 853 K, 873 K, 923 K, and 973 K, respectively. The sharp decline near 1033 K suggests an experimental T_c between 1033 and 1073 K, slightly lower than the predicted T_c range of 1091–1128 K from thermodynamic calculations in Fig. 6. This discrepancy is likely due to local compositional variations and non-equilibrium phase states not captured in simulations. The excellent high-temperature performance is attributed to the thermal stability of the Cu-rich phase within the supersaturated SS matrix, which effectively mitigates magnetic degradation at elevated temperatures [15].

The enhancement in magnetic properties is attributed to the microstructural evolution with increasing sintering temperature, as schematically illustrated in Fig. 18. At 973 K, the microstructure is heterogeneous, containing dispersed Ti-rich and Cu-rich phases that reflect limited atomic diffusion and significant elemental segregation. As the sintering temperature rises, accelerated diffusion promotes grain growth and interconnection. These elevated temperatures further facilitate grain coalescence and the formation of a continuous grain boundary network. By 1273 K, the microstructure transforms into a homogeneous polyhedral grain, indicating a high degree of densification and compositional uniformity. At this optimal temperature, the average grain size more than doubles compared to the structures obtained at 973 K and 1073 K.

The magnetic properties of the $Fe_{42}Co_{17}Ni_{12}Al_{17}Cu_6Ti_6$ HEA as a function of sintering temperature are summarized in Table 7. The sintering temperature had a pronounced influence on BH_{max}, which increased from 1.8 kJ/m^3 at 973 K to 4.4 kJ/m^3 at 1273 K, representing a 144 % improvement. The absence of Ti-rich phases at 1273 K confirms successful microstructural homogenization at this temperature. The achieved BH_{max} of 4.4 kJ/m^3 classifies the material as a semi-hard magnet. While this performance is promising for a rare-earth-free, as-sintered alloy, it remains below that of fully optimized commercial permanent magnets. The deficit is likely attributable to the lack of a post-sintering thermomagnetic treatment, which is typically employed in alloys like Alnico to induce magnetic anisotropy and enhance H_c.

For context, a benchmark Alnico 5 sample sintered under identical conditions but without thermomagnetic treatment exhibited a BH_{max} of 3.3 kJ/m^3. This value is substantially lower than the ~50 kJ/m^3 typical of commercially optimized, fully processed Alnico 5, underscoring the critical role of thermomagnetic treatment in driving spinodal decomposition and establishing magnetic texture. Notably, $Fe_{42}Co_{17}Ni_{12}Al_{17}Cu_6Ti_6$ HEA achieved a BH_{max} of 4.4 kJ/m^3 under the same untreated conditions, outperforming the Alnico 5 benchmark. This suggests that the intrinsic composition and resulting microstructure of the HEA are more favorable for developing useful magnetic properties in the as-sintered state, even in the absence of field annealing.

The observed increase in H_{cj} with sintering temperature is consistent with the pinning mechanisms described by Na et al. [34], where Cu-rich phases at grain boundaries act as pinning sites for domain walls, increasing H_c. While Na et al. focused on H_c, both H_{cj} and H_c are governed by domain wall pinning. In this HEA, increased densification is the primary driver of improved H_{cj} and BH_{max}, with a synergistic pinning effect likely resulting from Cu-rich phase distribution.

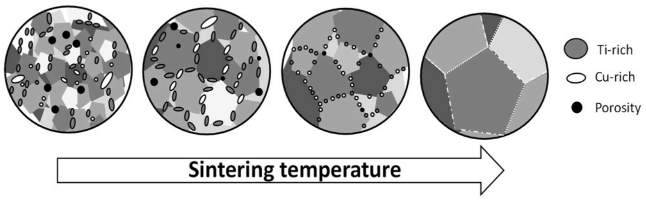

Fig. 18. Schematic evolution of microstructure in $Fe_{42}Co_{17}Ni_{12}Al_{17}Cu_6Ti_6$ HEA as a function of sintering temperature.

Table 7
Magnetic properties of the $Fe_{42}Co_{17}Ni_{12}Al_{17}Cu_6Ti_6$ as a function of sintering temperature and benchmark Alnico 5 at 1273 K.

Sintering temperature (K)	BH_{max} (kJ/m^3)	H_{cj} (kA/m)	H_{cb} (kA/m)	B_r (T)
973	1.8	23.2	21.5	0.28
1073	1.9	25.9	24.1	0.29
1173	2.6	31.9	29.3	0.29
1273	4.4	35.7	33.4	0.42
Alnico 5	3.3	30.3	27.9	0.45

Similarly, B_r increased from 0.28 T at 973 K to 0.42 T at 1273 K, indicating improved magnetization retention. Despite this improvement, the achieved values remain significantly lower than those of commercial NdFeB and Alnico magnets. This is attributed to the high concentration of non-magnetic elements (39 at%), which dilute the ferromagnetic Fe-Co-Ni matrix and reduce the effective magnetic volume. The observed gradual increase in B_r correlates with the progression of microstructural homogenization at higher sintering temperatures.

At lower sintering temperatures (973–1073 K), coarse phase segregation and residual porosity act as pinning sites that disrupt magnetic domain alignment, thereby degrading magnetic performance. In contrast, sintering at 1273 K enhances atomic diffusion, which eliminates Ti-rich secondary phases, significantly reduces porosity, and promotes the formation of a homogenous polyhedral grain structure. Consequently, a significant enhancement in magnetic properties, specifically the BH_{max} and B_r, was achieved at 1273 K. The improvement is attributed to the synergistic effects of increased density and the suppression of non-magnetic secondary phases, which collectively outweigh the minor detrimental effect of a broader grain size distribution.

4. Conclusions

This study developed a novel $Fe_{42}Co_{17}Ni_{12}Al_{17}Cu_6Ti_6$ HEA using a high-throughput CALPHAD-guided design framework integrated with statistical data analysis. The results demonstrate that promising magnetic performance can be achieved in as-sintered alloys with reduced Co and Ni content and a high fraction of non-magnetic elements. Compositional control was shown to be crucial for stabilizing the BCC_B2 phase and enhancing T_c.

The optimized alloy achieved its highest magnetic performance (BH_{max} = 4.4 kJ/m^3, H_{cj} = 35.7 kA/m, H_{cb} = 33.4 kA/m, and B_r = 0.42 T) at a sintering temperature of 1273 K, classifying it as a semi-hard magnet and a potential low-cost alternative to conventional Alnico-type magnets.

Beyond this material-specific outcome, the broader contribution of this work lies in demonstrating a scalable, thermodynamics-guided high-throughput methodology for magnetic materials discovery. By combining CALPHAD modeling, data-driven analysis, and experimental validation, the proposed framework enables rapid, resource-efficient exploration of complex compositional spaces while incorporating sustainability considerations.

Future research should focus on extending this framework through thermomagnetic processing, machine-learning integration, and lifecycle analysis to further optimize performance and sustainability. While this study primarily explored the Fe–Co–Ni–Al–Cu–Ti system, expanding the compositional scope and validating mechanical and thermal stability under service conditions will be essential to fully realize its potential. Overall, this work establishes a generalizable strategy for accelerating the design of next-generation sustainable magnetic materials.

CRediT authorship contribution statement

Garcia Jose Carlos: Validation, Methodology, Investigation, Formal analysis. **Lagos Miguel A.:** Writing – review & editing, Validation, Investigation, Formal analysis, Data curation, Conceptualization. **Sanchez Jon Mikel:** Writing – original draft, Validation, Software, Methodology, Investigation, Formal analysis, Data curation, Conceptualization. **Rivera Christian:** Validation, Supervision, Methodology, Investigation. **Checa Fernandez Blanca Luna:** Writing – review & editing, Supervision, Formal analysis. **Leizaola Iñaki:** Validation, Methodology, Investigation, Conceptualization.

Declaration of Competing Interest

The authors declare that they have no known competing financial interests or personal relationships that could have appeared to influence the work reported in this paper.

Acknowledgments

This work has been partially funded by The Provincial Council of Gipuzkoa through the project MATBIL (2023-CIEN-000054–01) and by the Basque Government through the project CIPEME (KK-2024/00053).

References

[1] D.B. Miracle, O.N. Senkov, A critical review of high entropy alloys and related concepts, Acta Mater. (2017), https://doi.org/10.1016/j.actamat.2016.08.081.

[2] C.K.H. Borg, C. Frey, J. Moh, T.M. Pollock, S. Gorsse, D.B. Miracle, O.N. Senkov, B. Meredig, J.E. Saal, Expanded dataset of mechanical properties and observed phases of multi-principal element alloys, 2020, pp. 1–6. https://doi.org/10.1038/s41597-020-00768-9.

[3] S. Gorsse, D.B. Miracle, O.N. Senkov, Mapping the world of complex concentrated alloys, Acta Mater. 135 (2017) 177–187, https://doi.org/10.1016/j.actamat.2017.06.027.

[4] E.P. George, W.A. Curtin, C.C. Tasan, High entropy alloys: a focused review of mechanical properties and deformation mechanisms, Acta Mater. 188 (2020) 435–474, https://doi.org/10.1016/j.actamat.2019.12.015.

[5] Y.Y. Chen, U.T. Hong, H.C. Shih, J.W. Yeh, T. Duval, Electrochemical kinetics of the high entropy alloys in aqueous environments—a comparison with type 304 stainless steel, Corros. Sci. 47 (2005) 2679–2699, https://doi.org/10.1016/J.CORSCI.2004.09.026.

[6] P. Kumari, S.K. Mohapatra, P. Yadav, R.J. Choudhary, A. Lakhani, R.R. Shahi, Integrative approach to enhance the soft magnetic properties of Co35Cr5Fe10Ni30Ti20-xAlx (x= 10, 15, 20) high entropy alloys, J. Alloy. Compd. 1005 (2024) 175890, https://doi.org/10.1016/j.jallcom.2024.175890.

[7] Y.F. Kao, S.K. Chen, T.J. Chen, P.C. Chu, J.W. Yeh, S.J. Lin, Electrical, magnetic, and Hall properties of AlxCoCrFeNi high-entropy alloys, J. Alloy. Compd. 509 (2011) 1607–1614, https://doi.org/10.1016/J.JALLCOM.2010.10.210.

[8] B.S. Murty, J.W. Yeh, S. Ranganathan, Applications and future directions, High. Entropy Alloy (2014) 159–169, https://doi.org/10.1016/B978-0-12-800251-3.00010-9.

[9] W.J. Ripple, C. Wolf, J.W. Gregg, J. Rockström, M.E. Mann, N. Oreskes, T. M. Lenton, S. Rahmstorf, T.M. Newsome, C. Xu, J.-C. Svenning, C.C. Pereira, B. E. Law, T.W. Crowther, The 2024 state of the climate report: Perilous times on planet Earth, Bioscience 74 (2024) 812–824, https://doi.org/10.1093/biosci/biae087.

[10] S. Sugimoto, in: K. Fujisaki (Ed.), History and Future of Soft and Hard Magnetic Materials BT - Magnetic Material for Motor Drive Systems: Fusion Technology of Electromagnetic Fields, Springer Singapore, Singapore, 2019, pp. 261–277, https://doi.org/10.1007/978-981-32-9906-1_18.

[11] P. Zapp, A. Schreiber, J. Marx, W. Kuckshinrichs, Environmental impacts of rare earth production, MRS Bull. 47 (2022) 267–275, https://doi.org/10.1557/s43577-022-00286-6.

[12] D.H. Dang, K.A. Thompson, L. Ma, H.Q. Nguyen, S.T. Luu, M.T.N. Duong, A. Kernaghan, Toward the circular economy of rare earth elements: a review of abundance, extraction, applications, and environmental impacts, Arch. Environ. Contam. Toxicol. 81 (2021) 521–530, https://doi.org/10.1007/s00244-021-00867-7.

[13] P.F. Yu, L.J. Zhang, H. Cheng, H. Zhang, M.Z. Ma, Y.C. Li, G. Li, P.K. Liaw, R.P. Liu, The high-entropy alloys with high hardness and soft magnetic property prepared by mechanical alloying and high-pressure sintering, Intermetallics 70 (2016) 82–87, https://doi.org/10.1016/j.intermet.2015.11.005.

[14] C. Liu, W. Peng, C.S. Jiang, H. Guo, J. Tao, X. Deng, Z. Chen, Composition and phase structure dependence of mechanical and magnetic properties for AlCoCuFeNi x high entropy alloys, J. Mater. Sci. Technol. 35 (2019) 1175–1183, https://doi.org/10.1016/j.jmst.2018.12.014.

[15] L. Han, Z. Rao, I.R. Souza Filho, F. Maccari, Y. Wei, G. Wu, A. Ahmadian, X. Zhou, O. Gutfleisch, D. Ponge, D. Raabe, Z. Li, Ultrastrong and ductile soft magnetic high-entropy alloys via coherent ordered nanoprecipitates, Adv. Mater. 33 (2021), https://doi.org/10.1002/adma.202102139.

[16] L. Han, F. Maccari, I.R. Souza Filho, N.J. Peter, Y. Wei, B. Gault, O. Gutfleisch, Z. Li, D. Raabe, A mechanically strong and ductile soft magnet with extremely low coercivity, Nature 608 (2022) 310–316, https://doi.org/10.1038/s41586-022-04935-3.

[17] Y. Ye, S.D. Lish, L. Xu, E. Woods, S. Chen, Y. Ren, M.W. Wittmann, H. Xu, B. Gault, I. Baker, Exceptional soft magnetic properties of an ordered multi-principal element alloy with disordered nanoprecipitates, High. Entropy Alloy. Mater. 1 (2023) 165–174, https://doi.org/10.1007/s44210-022-00010-8.

[18] T. Borkar, V. Chaudhary, B. Gwalani, D. Choudhuri, C.V. Mikler, V. Soni, T. Alam, R. V. Ramanujan, R. Banerjee, A combinatorial approach for assessing the magnetic properties of high entropy alloys: role of Cr in AlCoxCr1–xFeNi, Adv. Eng. Mater. 19 (2017) 1–13, https://doi.org/10.1002/adem.201700048.

[19] R. Gong, Q. Yang, W. Wu, P. Ge, S. Zhu, W. Zhang, D. Yan, Z. Li, Green multicomponent alloys with excellent multifunctional and mechanical properties, Adv. Eng. Mater. (2025), https://doi.org/10.1002/adem.202402307.

[20] M. Takeuchi, Y. Iwama, Effects of titanium upon magnetic anisotropy and coercivity in alnico magnet alloys, Trans. Jpn. Inst. Met. 17 (1976) 489–496, https://doi.org/10.2320/MATERTRANS1960.17.489.

[21] H. Liu, S.U. Rehman, Y. Deng, Z. Liu, X. Yu, M. Yang, Evolution of microstructure and magnetic properties of isotropic alnico 8 ribbons with various Ti contents, J. Supercond. Nov. Magn. 37 (2024) 791–798, https://doi.org/10.1007/s10948-024-06718-5.

[22] S.U. Rehman, C. Wei, R. Zhang, H. Liu, S. Li, Z. Minglong, M. Yang, Q. Jiang, J. Wang, Z. Zhong, Tailoring the magnetic properties and microstructure of Alnico 8 magnets by various Ti contents and processing conditions, Intermetallics 143 (2022) 107486, https://doi.org/10.1016/j.intermet.2022.107486.

[23] X. Yu, S.Y. Chen, F. Gu, Z.Y. Zhang, J.B. Sun, C.X. Cui, Preparation of Alnico magnet with high magnetization by thermal deformation, Mater. Lett. 310 (2022) 131503, https://doi.org/10.1016/j.matlet.2021.131503.

[24] L. Zhou, W. Tang, L. Ke, W. Guo, J.D. Poplawsky, I.E. Anderson, M.J. Kramer, Microstructural and magnetic property evolution with different heat-treatment conditions in an alnico alloy, Acta Mater. 133 (2017) 73–80, https://doi.org/10.1016/j.actamat.2017.05.012.

[25] L. Zhou, M.K. Miller, P. Lu, L. Ke, R. Skomski, H. Dillon, Q. Xing, A. Palasyuk, M. R. McCartney, D.J. Smith, S. Constantinides, R.W. McCallum, I.E. Anderson, V. Antropov, M.J. Kramer, Architecture and magnetism of alnico, Acta Mater. 74 (2014) 224–233, https://doi.org/10.1016/j.actamat.2014.04.044.

[26] R.A. McCurrie, The structure and properties of alnico permanent magnet alloys, Handb. Ferromagn. Mater. 3 (1982) 107–109, https://doi.org/10.1016/S1574-9304(05)80089-6.

[27] S.U. Rehman, Z. Ahmad, A. ul Haq, S. Akhtar, Effects of Zr alloying on the microstructure and magnetic properties of Alnico permanent magnets, J. Magn. Magn. Mater. 442 (2017) 136–140, https://doi.org/10.1016/j.jmmm.2017.06.114.

[28] R. Kulkarni, B.S. Murty, V. Srinivas, Study of microstructure and magnetic properties of AlNiCo(CuFe) high entropy alloy, J. Alloy. Compd. 746 (2018) 194–199, https://doi.org/10.1016/j.jallcom.2018.02.275.

[29] S.S. Nene, S. Sinha, D.K. Yadav, A. Dutta, Metallurgical aspects of high entropy alloys, J. Alloy. Compd. 1005 (2024) 175849, https://doi.org/10.1016/j.jallcom.2024.175849.

[30] Z. Rao, B. Dutta, F. Körmann, W. Lu, X. Zhou, C. Liu, A.K. da Silva, U. Wiedwald, M. Spasova, M. Farle, D. Ponge, B. Gault, J. Neugebauer, D. Raabe, Z. Li, Beyond solid solution high-entropy alloys: tailoring magnetic properties via spinodal decomposition, Adv. Funct. Mater. 31 (2021), https://doi.org/10.1002/adfm.202007668.

[31] H. Chen, J. Gou, W. Jia, X. Song, T. Ma, Origin of hard magnetism in Fe-Co-Ni-Al-Ti-Cu high-entropy alloy: chemical shape anisotropy, Acta Mater. 246 (2023) 118702, https://doi.org/10.1016/j.actamat.2023.118702.

[32] S. Pourmohammadi, A. Mohammadnejad, A. Bahrami, S.H.M. Anijdan, N. Park, M. Ghosh, metals Article Phase Stability, Microstructure, and Mechanical Properties of Spark Plasma Sintered Nanocrystalline Boron-Doped AlCoFeMnNi High-Entropy Alloy, 2023. https://doi.org/10.3390/met13061025.

[33] Q. Lan, A. Kovács, J. Caron, H. Du, D. Song, S. Dasari, B. Gwalani, V. Chaudhary, R. V. Ramanujan, R. Banerjee, R.E. Dunin-Borkowski, Highly complex magnetic behavior resulting from hierarchical phase separation in AlCo(Cr)FeNi high-entropy alloys, IScience 25 (2022), https://doi.org/10.1016/j.isci.2022.104047.

[34] S.M. Na, P.K. Lambert, N.J. Jones, Hard magnetic properties of FeCoNiAlCuXTiXbased high entropy alloys, AIP Adv. 11 (2021), https://doi.org/10.1063/9.0000097.

[35] C. Yang, J. Zhang, M. Li, X. Liu, Soft-magnetic high-entropy AlCoFeMnNi alloys with dual-phase microstructures induced by annealing, Acta Metall. Sin. Engl. Lett. 33 (2020) 1124–1134, https://doi.org/10.1007/s40195-020-01086-0.

[36] K. Için, Investigation of phase transformation related magnetic properties of Ti addition to FeCoCuNiMn and FeCoCuNiAl high entropy alloys by vacuum arc melting, Mater. Today Commun. 39 (2024), https://doi.org/10.1016/j.mtcomm.2024.108821.

[37] P. Nieves, S. Arapan, J. Maudes-Raedo, R. Marticorena-Sánchez, N.L. Del Brío, A. Kovacs, C. Echevarria-Bonet, D. Salazar, J. Weischenberg, H. Zhang, O. Y. Vekilova, R. Serrano-López, J.M. Barandiaran, K. Skokov, O. Gutfleisch, O. Eriksson, H.C. Herper, T. Schrefl, S. Cuesta-López, Database of novel magnetic materials for high-performance permanent magnet development, Comput. Mater. Sci. 168 (2019) 188–202, https://doi.org/10.1016/j.commatsci.2019.06.007.

[38] J. Mohapatra, X. Liu, P. Joshi, J.P. Liu, Hard and semi-hard Fe-based magnetic materials, J. Alloy. Compd. 955 (2023) 170258, https://doi.org/10.1016/j.jallcom.2023.170258.

[39] K.L.S. Rodríguez, J.J.M. Quintero, C.E. Rodríguez Torres, L. Errico, Structural, electronic, magnetic and hyperfine properties of Fe2AlO4 and FeAl2O4. A DFT study, J. Alloy. Compd. 958 (2023) 170385, https://doi.org/10.1016/j.jallcom.2023.170385.

[40] Y. Magnin, K. Akabli, H.T. Diep, I. Harada, Monte Carlo study of the spin transport in magnetic materials, Comput. Mater. Sci. 49 (2010) S204–S209, https://doi.org/10.1016/j.commatsci.2010.02.011.

[41] H. Chen, Y. Zhai, J.J. Turner, A. Feiguin, A high-performance implementation of atomistic spin dynamics simulations on x86 CPUs, Comput. Phys. Commun. 291 (2023) 108851, https://doi.org/10.1016/j.cpc.2023.108851.

[42] B.G. del Rio, B. Phan, R. Ramprasad, A deep learning framework to emulate density functional theory, Npj Comput. Mater. 9 (2023) 158, https://doi.org/10.1038/s41524-023-01115-3.

[43] Z. Yuan, Z. Xu, H. Li, X. Cheng, H. Tao, Z. Tang, Z. Zhou, W. Duan, Y. Xu, Equivariant neural network force fields for magnetic materials, Quantum Front. 3 (2024) 8, https://doi.org/10.1007/s44214-024-00055-3.

[44] A.S. Kotykhov, K. Gubaev, M. Hodapp, C. Tantardini, A.V. Shapeev, I.S. Novikov, Constrained DFT-based magnetic machine-learning potentials for magnetic alloys: a case study of Fe–Al, Sci. Rep. 13 (2023) 19728, https://doi.org/10.1038/s41598-023-46951-x.

[45] S. Mooraj, W. Chen, A review on high-throughput development of high- entropy alloys by combinatorial methods, 2023. https://doi.org/10.20517/jmi.2022.41.

[46] Y. Zeng, M. Man, C. Koon Ng, Z. Aitken, K. Bai, D. Wuu, J. Jun Lee, S. Rong Ng, F. Wei, P. Wang, D. Cheng Cheh Tan, Y.W. Zhang, Search for eutectic high entropy alloys by integrating high-throughput CALPHAD, machine learning and experiments, Mater. Des. 241 (2024) 112929, https://doi.org/10.1016/j.matdes.2024.112929.

[47] R. Feng, C. Zhang, M.C. Gao, Z. Pei, F. Zhang, Y. Chen, D. Ma, K. An, J. D. Poplawsky, L. Ouyang, Y. Ren, J.A. Hawk, M. Widom, P.K. Liaw, High-throughput design of high-performance lightweight high-entropy alloys, Nat. Commun. 12 (2021) 6–15, https://doi.org/10.1038/s41467-021-24523-9.

[48] J.M. Sanchez, H. Galarraga, I. Marquez, M.G. de Cortazar, High-throughput CALPHAD-guided design and experimental study on the development of a novel multicomponent as-cast Al-Si-Cu-Zn-Fe-Mn-Mg based alloy through the direct melting of post-consumer scrap, J. Alloy. Compd. (2025) 178888, https://doi.org/10.1016/J.JALLCOM.2025.178888.

[49] L. Han, Z. Sun, W. Xia, S.P. Tsai, X. Zhang, J. Rao, P. Wang, A.C.Y. Ngo, Z. Li, Y. Liu, D. Raabe, Thermodynamics-guided high-throughput discovery of eutectic high-entropy alloys for rapid solidification, Adv. Sci. 11 (2024) 1–9, https://doi.org/10.1002/advs.202401559.

[50] E. Ghassemali, P.L.J. Conway, High-throughput CALPHAD: a powerful tool towards accelerated metallurgy, Front. Mater. 9 (2022) 1–7, https://doi.org/10.3389/fmats.2022.889771.

[51] J.J. Mason, D.W. Ashall, A.V. Dean, The structure of Ni-Co-Al-Ti-Cu-Fe permanent magnets, IEEE Trans. Magn. 6 (1970) 191–194, https://doi.org/10.1109/TMAG.1970.1066744.

[52] T. Yang, Y. Zhao, W. Liu, J. Kai, C. Liu, L12-strengthened high-entropy alloys for advanced structural applications, J. Mater. Res. 33 (2018) 2983–2997, https://doi.org/10.1557/jmr.2018.186.

[53] K. Ishikawa, I. Ohnuma, R. Kainuma, K. Aoki, K. Ishida, Phase equilibria and stability of Heusler-type aluminides in the NiAl–Ni2AlTi–Ni2AlY (Y: V, Cr or Mn) systems, J. Alloy. Compd. 367 (2004) 2–9, https://doi.org/10.1016/j.jallcom.2003.08.002.

[54] K. Xu, C. Zhan, M. Lou, X. Xiao, R. Zhou, F. Wang, X. Hu, Y. Yuan, K. Chang, Design of the rare-earth-containing materials based on the micro-alloying phase equilibria, phase diagrams and phase transformations, J. Mater. Sci. Technol. 151 (2023) 119–149, https://doi.org/10.1016/j.jmst.2022.11.056.

[55] J.O. Andersson, T. Helander, L. Höglund, P. Shi, B. Sundman, Thermo-Calc & DICTRA, computational tools for materials science, Calphad Comput. Coupl. Ph. Diagr. Thermochem 26 (2002) 273–312, https://doi.org/10.1016/S0364-5916(02)00037-8.

[56] B.S. Murty, J.W. Yeh, S. Ranganathan, P.P. Bhattacharjee, Physical metallurgy of high-entropy alloys, High. Entropy Alloy (2019) 31–50, https://doi.org/10.1016/b978-0-12-816067-1.00003-5.

[57] M.C. Gao, C. Zhang, P. Gao, F. Zhang, L.Z. Ouyang, M. Widom, J.A. Hawk, Thermodynamics of concentrated solid solution alloys, Curr. Opin. Solid State Mater. Sci. 21 (2017) 238–251, https://doi.org/10.1016/j.cossms.2017.08.001.

[58] S. Guo, C. Ng, J. Lu, C.T. Liu, Effect of valence electron concentration on stability of fcc or bcc phase in high entropy alloys, J. Appl. Phys. 109 (2011), https://doi.org/10.1063/1.3587228/984570.

[59] H. Luan, Z. Zhao, Y. Liu, L. Liu, M. Huang, B. Zhou, Y. Ding, J. Zhao, Y. Sun, A. Yan, Effect of grain structure on the magnetic properties of AlNiCo 8 alloys, Mater. Today Commun. 40 (2024) 109844, https://doi.org/10.1016/j.mtcomm.2024.109844.

[60] H. Luan, Z. Zhao, Y. Liu, M. Huang, L. Liu, Y. Ding, A. Yan, Y. Sun, J. Zhao, Grain growth mechanism of AlNiCo magnetic alloy under different withdrawal rates, J. Alloy. Compd. 1029 (2025) 180853, https://doi.org/10.1016/j.jallcom.2025.180853.

[61] J. Liu, J. Wilson, C.L. Davis, A. Peyton, Magnetic characterisation of grain size and precipitate distribution by major and minor BH loop measurements, J. Magn. Magn. Mater. 481 (2019) 55–67, https://doi.org/10.1016/j.jmmm.2019.02.088.

[62] N. Leuning, S. Steentjes, K. Hameyer, Impact of grain size distribution on the magnetic deterioration due to cutting of electrical steel sheets, J. Magn. Magn. Mater. 497 (2020) 166080, https://doi.org/10.1016/j.jmmm.2019.166080.

[63] L. Zhou, W. Tang, L. Ke, W. Guo, J.D. Poplawsky, I.E. Anderson, M.J. Kramer, Microstructural and magnetic property evolution with different heat-treatment conditions in an alnico alloy, Acta Mater. 133 (2017) 73–80, https://doi.org/10.1016/j.actamat.2017.05.012.

[64] Y. Zhang, Y.J. Zhou, J.P. Lin, G.L. Chen, P.K. Liaw, Solid-solution phase formation rules for multi-component alloys, Adv. Eng. Mater. 10 (2008) 534–538, https://doi.org/10.1002/adem.200700240.

[65] R. Kobayashi, Y. Mitsui, R.Y. Umetsu, K. Takahashi, K. Koyama, Acceleration of B2/L21 order-disorder transformation in Ni2MnAl Heusler alloys by in-magnetic-field annealing, J. Magn. Magn. Mater. 547 (2022) 168908, https://doi.org/10.1016/j.jmmm.2021.168908.

[66] J. Millán, S. Sandlöbes, A. Al-Zubi, T. Hickel, P. Choi, J. Neugebauer, D. Ponge, D. Raabe, Designing Heusler nanoprecipitates by elastic misfit stabilization in Fe–Mn maraging steels, Acta Mater. 76 (2014) 94–105, https://doi.org/10.1016/j.actamat.2014.05.016.

[67] S.B. Park, Heterogeneous nucleation models to predict grain size in solidification, Prog. Mater. Sci. 123 (2022) 100822, https://doi.org/10.1016/j.pmatsci.2021.100822.

[68] M. Haseeb, H. Zhang, Y. Li, P. Zhang, Z. Geng, M. Yue, Sintering temperature optimization for enhanced magnetic performance in La-Ca-Co doped strontium ferrite, AIP Adv. 14 (2024) 25204, https://doi.org/10.1063/9.0000653/3261701.

[69] S. Garehbaghi, A. Kianvash, Effect of various parameters on the microstructure and magnetic properties of sintered Sr-hexaferrite, Results Phys. 12 (2019) 1559–1568, https://doi.org/10.1016/j.rinp.2019.01.038.

[70] Z.W. Li, G.Q. Lin, L. Chen, Y.P. Wu, C.K. Ong, Size effect on the static and dynamic magnetic properties of W -type barium ferrite composites: from microparticles to nanoparticles, J. Appl. Phys. 98 (2005), https://doi.org/10.1063/1.2128688/924633.

[71] D. Jiles, Introd. Magn. Magn. Mater. (2015), https://doi.org/10.1201/B18948.

[72] A. Fourmont, A.S. Rogachev, S. Le Gallet, O. Politano, D.Y. Kovalev, N.A. Kochetov, N.F. Shkodich, S.G. Vadchenko, F. Baras, Thermal stability of medium- and high-entropy alloys of 3d-transition metals, J. Ph. Equilib. Diffus 42 (2021) 720–734, https://doi.org/10.1007/s11669-021-00903-y.